

Original article

Mechanical characterization of uniaxial compression associated with lamination angles in shale

Ming Gao¹, Manping Yang¹*, Yanjun Lu¹, V. A. Levin², Pei He³, Hongjian Zhu¹*

¹School of Vehicle and Energy, Yanshan University, Qinhuangdao 066000, P. R. China

²Department of Mechanics and Mathematics, Lomonosov Moscow State University, Moscow 119991, Russian Federation

³Key Laboratory of Shale Gas Exploration, Ministry of Natural Resources, Chongqing Institute of Geology and Mineral Resources, Chongqing 401120, P. R. China

Keywords:

Shale
crack
fractal theory
uniaxial compression
CT scanning

Cited as:

Gao, M., Yang, M., Lu, Y., Levin, V. A., He, P., Zhu, H. Mechanical characterization of uniaxial compression associated with lamination angles in shale. *Advances in Geo-Energy Research*, 2024, 13(1): 56-68.
<https://doi.org/10.46690/ager.2024.07.07>

Abstract:

This paper investigates the mechanical properties and damage laws of marine shale from the Silurian Longmaxi Formation by conducting uniaxial compression experiments with varying lamination angles with respect to the loading direction. Data are analyzed via computed tomography scanning and fractal theory to reveal a series of mechanical properties, considering stress-strain curve, compressive strength, Young's modulus, and Poisson's ratio. The results indicate three damage modes in shale samples: shear, tension-shear, and tension. The shales are anisotropic as the mechanical properties vary with the lamination orientation and the loading direction. The compressive strength decreases non-linearly with increasing lamination angle, whereas the Young's modulus and Poisson's ratio correlate almost linearly with the lamination angle. To overcome the defect of visual images when quantitatively evaluating cracks and rock damage to investigate the mechanical properties of shale, we propose block fractal dimension and crack fractal dimensions calculated using post-experimental photographs and computed tomography images. Fractal dimensions are useful tools for identifying variations in uniaxial compressive strength and correlate positively with the sample damage, particularly their damage class. This study highlights the value of applying fractal theory for the quantitative characterization of shale mechanical properties, and reveals that the lamination orientation to the loading direction is a parameter that significantly controls the mechanical properties of shale.

1. Introduction

Shale is characterized microscopically by pore size in the nanometer range, low porosity (less than 10%), and low permeability (under 0.5 millidarcies) (Sarout et al., 2007; Zhao et al., 2019; Zhu et al., 2021), parameters that can directly control shale gas content in place and determine the production techniques. In the Sichuan Basin, South China, the Longmaxi shale of Silurian age is commonly known as significant reservoir rocks for shale gas. This formation includes a wide range of organic-rich argillaceous rocks with widely varying compositions and hydration states and thinly laminated fabrics (Gao et al., 2023; Zhao et al., 2023), while little is known regarding how the rock mechanical characteristics depend on

the variation of petrophysical properties.

Experimental studies of organic-rich shales of various mineral compositions have established that the mechanical properties of these shales are strongly dependent on confining pressure, temperature, strain rate, water content, and original rock fabric (e.g., sedimentary laminations) (Rybacki et al., 2015; Liu et al., 2020; Su et al., 2022). The mechanical properties of lamination shale are anisotropic, as demonstrated by earlier research involving mechanical compression tests under various lamination angles ranging from 0° to 90° (Arora and Mishra, 2015; Marie et al., 2019; Li et al., 2022). Sethi et al. (2024) determined the brittleness index and used Brazilian splitting to test the tensile strength and mechanical characteristics of shale. This foundation has allowed numerous

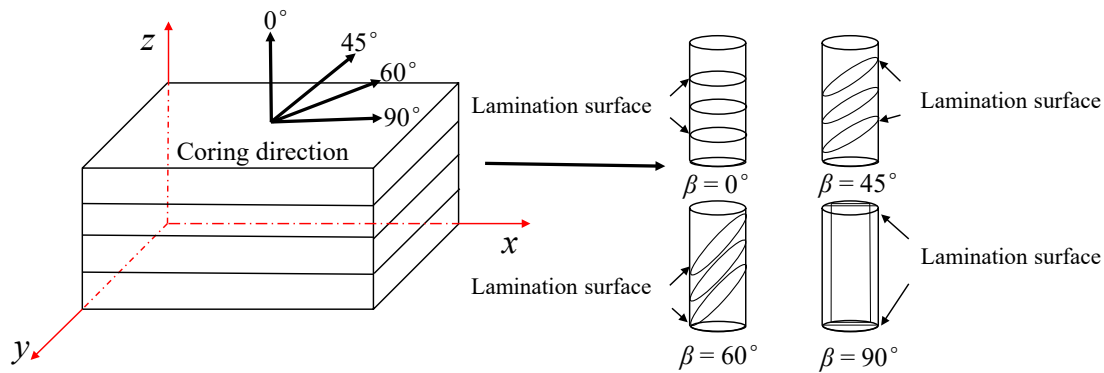


Fig. 1. Coring schematic diagram.

scholars to conduct Brazilian splitting tests while taking into account varying shale lamination angles and investigate the anisotropy brought on by shale lamination under Brazilian splitting. A further study used via computed tomography (CT) scanning in conjunction with uniaxial cyclic stress to describe the mechanical characteristics and crack laws of shale (Zhu et al., 2021; Li et al., 2023). The mechanical properties of lamination shale were examined in certain studies by combining tests for Brazilian splitting, uniaxial compression and triaxial compression (Marie et al., 2019; Niloufar and Fatemeh, 2023; Sethi et al., 2024). The conventional Euclidean space geometry theory, which has numerous drawbacks, form the basis of the majority of conclusions and study findings of rock mechanical experiments (Arora and Mishra, 2015; Alex and Ahamd, 2017; Marie et al., 2019). It is often relatively difficult to describe the intricate damage features of the aforementioned rocks. The development of fractal geometry theory and its application for rock mechanical research have given academics a fresh perspective on investigating the evolution law of rock damage in the face of these issues (Mandelbrot, 1983; Rickman et al., 2008).

Most studies have demonstrated the statistical self-similarity of intricate structures within the rock and their damage characteristics after loading at a particular scale (Velde et al., 1991; Bagde et al., 2002; Rickman et al., 2008). These structures are intimately associated with the damage process and the nature of the rock. The evolution of damage and deformation of rock mass under external load is a highly significant subject of investigation. Bagde et al. (2002) first developed a technique flow for the block fractal characterization of rock and presented fractal theory as a more dependable approach for rock characterization. Wang et al. (2023) examined granite fragments created during mechanical testing and computed the fractal dimension to examine the block varied fractal properties based on earlier research. The results revealed high regularity in the block fractal dimension subjected to mechanical tests. Fractal dimension and rock quality are connected (Amir et al., 2014). In addition, a significant number of intricate crack networks are also produced by the rock under loading. The fractal dimension characterization of rock damage has been performed in the past by combining fractal theory with digital image processing technology (Xiao et al., 2024). However, the majority of these study objects for fractal theory are composed

of homogeneous rocks, such as granite and limestone, while the mechanical properties of heterogeneous strong shale have not been thoroughly studied using fractal theory.

Herein, we document the experimental results of rock deformation and the mechanical properties of Silurian Longmaxi shale under several lamination angles in relation to the loading direction (0° , 45° , 60° and 90°). Structural information for the experimentally deformed shale samples is derived from the combined results of post-experimental photographs, CT scanning, and fractal theory. Our three aims are to (1) observe the variations in damage modes among experimentally deformed shale samples, (2) discuss the impact of lamination angle with respect to the loading direction on the mechanical parameters of shale and (3) quantitatively evaluate the cracks, strength and mechanical characteristics of samples using both the block and crack fractal dimensions.

2. Samples and methods

2.1 Samples

The samples were collected from the outcrop black shale of the Silurian Longmaxi Formation, southern Sichuan Basin, which is characterized by obvious laminations. To investigate the variations in the mechanical properties of shale coring in various orientations, the varying lamination angles with respect to the loading direction were set to 0° , 45° , 60° and 90° . The size of samples was $50 \text{ mm} \times 100 \text{ mm}$, and the parallelism of the upper and lower surfaces was controlled at 0.03 mm . Complete black shale samples were selected to carry out an experimental study of rock mechanics (Fig. 1). A total of 12 shale samples based on varying lamination angles (0° , 45° , 60° and 90°) were divided into three groups: A, B and C. The basic parameters of the samples are shown in Table 1.

2.2 Experimental methods

The shale uniaxial compression experiment of this study used the TAW-2000 high-temperature and high-pressure triaxial experimental machine (Fig. 2) developed by Chaoyang Test Instrument Co., Ltd. (Changchun, China). This configuration has an axial pressure system, peripheral pressure system and pore water system, and is capable of carrying out uniaxial compressive strength test, Brazilian splitting experiment, room temperature/high temperature triaxial compressive strength test

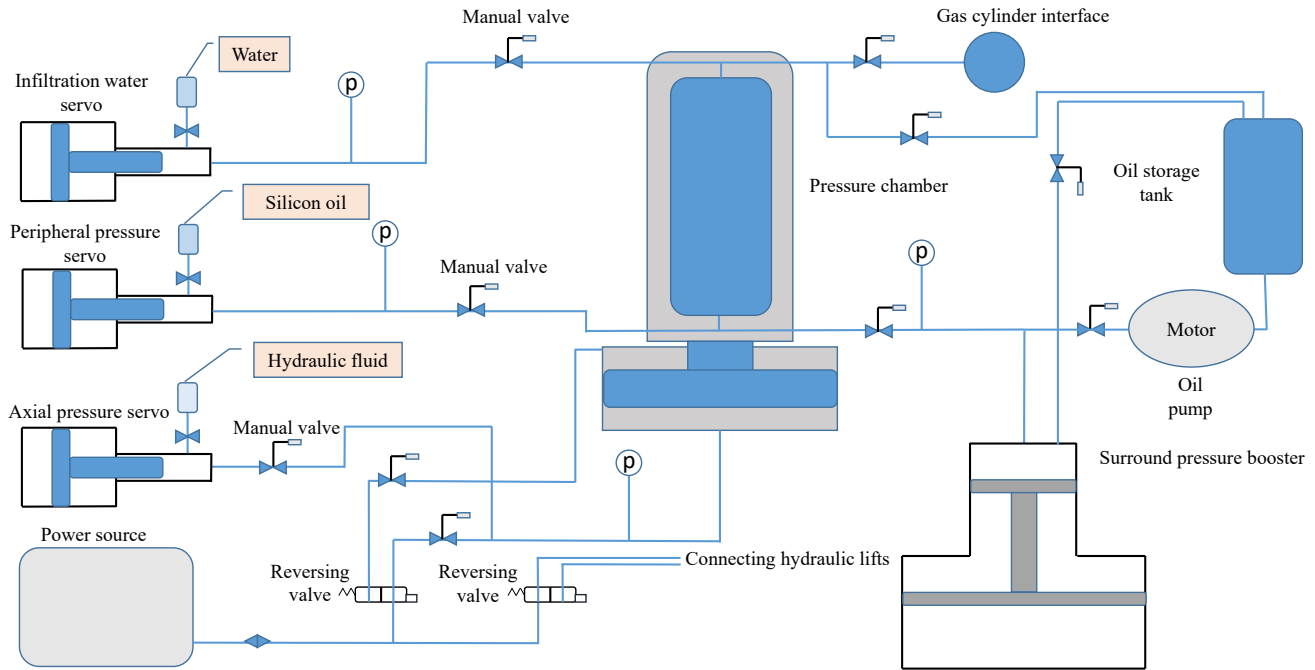


Fig. 2. Schematic diagram of the high-temperature and high-pressure triaxial testing machine TAW-2000.

Table 1. Basic parameters of the samples.

Sample	Lamination angle ($^{\circ}$)	Size (mm 2)	Mass (g)
A1	0	49.95 \times 100.50	510.723
A2	45	49.82 \times 100.64	508.195
A3	60	49.66 \times 100.32	498.426
A4	90	49.75 \times 99.99	503.474
B1	0	49.88 \times 100.59	502.489
B2	45	49.88 \times 100.59	505.563
B3	60	49.82 \times 100.44	501.222
B4	90	49.47 \times 100.54	504.406
C1	0	49.87 \times 100.45	511.499
C2	45	50.01 \times 100.43	507.327
C3	60	49.37 \times 100.35	496.296
C4	90	49.72 \times 100.90	502.585

st, rheological experiment, and hydraulic fracturing simulation experiment. The specific parameters of this instrument are as follows: Maximum axial load of 2,000 KN; experimental load accuracy: $\pm 1\%$; circumferential pressure accuracy: $\pm 2\%$; deformation accuracy: 0.001 mm; temperature control accuracy: $\pm 1\%$; measurable deformation range of the sample: axial for 0 ~ 10 mm, radial for 0 ~ 5 mm. This device can perfectly complete the mechanical experiments with high testing accuracy.

The CT scanning experiments were all completed by the X-ray detection equipment GE Phoenix V|tome|X S240 CT by Youer Hongxin Testing Technology (Shenzhen) Co., Ltd.

The specific parameters of this equipment are as follows: Maximum tube voltage, power: 240 KV, 320 W; minimum voxel: 1 micron; ensemble magnification: 1.46-100 \times , nanometer; the focus ray tube can reach 200 \times ; detail resolution: Up to < 1 micron; maximum sample weight: 10 kg. The equipment is capable of rapid data collection and three-dimensional reconstruction, in addition to robust data analysis, two- and three-dimensional detection, and detection of samples.

3. Results and Discussion

3.1 Damage law of shale

The first principal stress loading direction under uniaxial compression conditions is perpendicular to the lamination surface when $\beta = 0^{\circ}$ (Fig. 3). When the axial load induces radial deformation on the lamination surface, it first sprouts, then expands and eventually forms through the cracks. The form of destruction is along the lamination surface of the tensile damage. When $\beta = 45^{\circ}$, the shale sample fails due to radial tensile damage as well as shear damage along the lamination surface, as the lamination surface is at an angle of 45° with the axial load. It can be clearly observed that when $\beta = 60^{\circ}$, the shale sample produces a shear crack throughout. This occurs because the load acting on the lamination surface causes interlaminar friction, where the compressive and tensile strengths of the lamination surface are significantly lower than those of other surfaces. Therefore, the sample is prone to shear damage along the lamination angle. At $\beta = 90^{\circ}$, the axial load is parallel to the lamination surface, and the damage form is shearing damage parallel to the loading direction. Therefore, a weak faceted structure during the damage process is evidenced by shale microcracks, pores, mineral interstices, and others along the lamination direction under uniaxial compression cir-

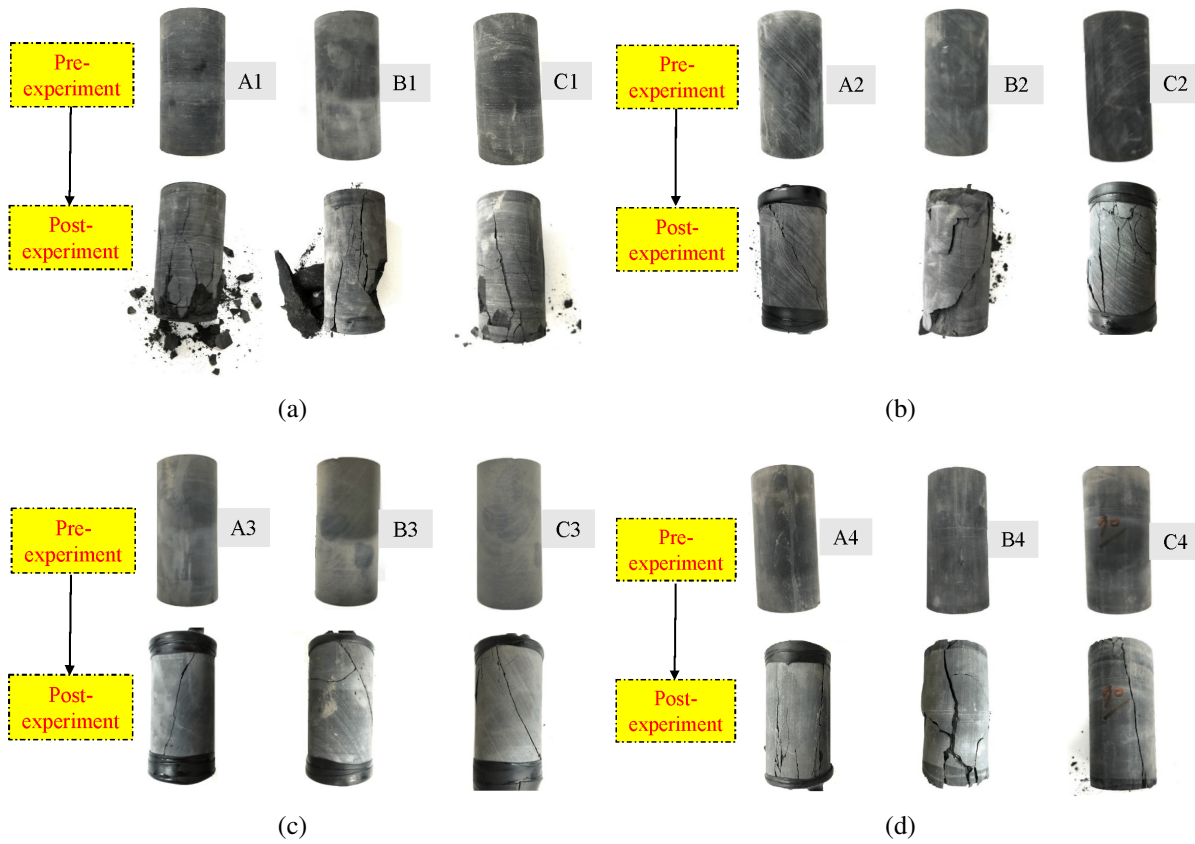


Fig. 3. Photographs of samples at (a) $\beta = 0^\circ$, (b) $\beta = 45^\circ$, (c) $\beta = 60^\circ$ and (d) $\beta = 90^\circ$ before and after the test.

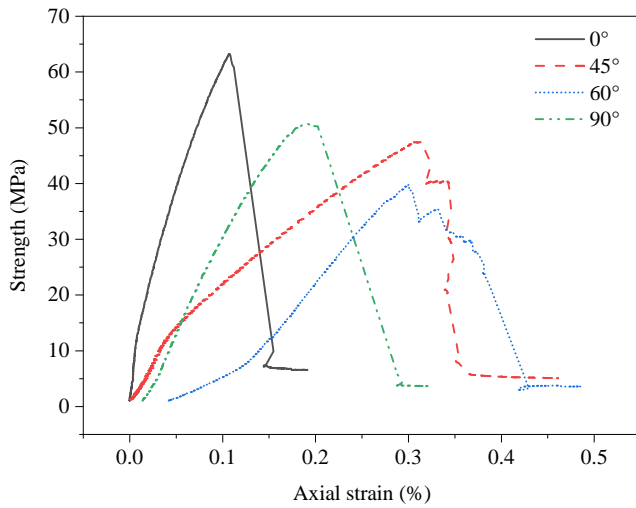


Fig. 4. Stress-strain curves of shale in uniaxial compression experiments.

cumstances, when they are more prone to produce cracks.

3.2 Stress-strain curve of shale

Four typical lamination angle shale samples were selected for the uniaxial compression test, and their stress-strain curves are presented in Fig. 4.

The type of stress-strain curve of this shale sample belongs to class II, which indicates that this shale sample is of brittle

rock type and undergoes five stages of change. During the first stage, the microcracks of the shale sample close under load, representing the compacting stage. Then, the shale sample experiences a rather long elastic phase during which few new microcracks are created and the curve slope is nearly constant, demonstrating clear linear elasticity. Next, a number of microcracks typically form near the lamination surface of the shale sample. In addition, the slope of the curve decreases as the strain increases. The sample deformation gradually shifts from elasticity to elasticity-plasticity in this stage. Subsequently, the shale sample experiences a stage of plastic damage characterized by an elevated number of microcracks pointing in a specific direction. Then, a macroscopic rupture will result from the linking of these microcracks. The shale sample still exhibits some resistance to deformation after cracking, comprising the residual strength stage.

These five stages are in general agreement with those obtained by previous researchers, while the stress-strain curves of shale in these studies do not have any obvious residual strength stage (Arora and Mishra, 2015; Niloufar and Fatemeh, 2023). The possible reason is that the experiment of this paper continued loading until the compressive strength remained unchanged. Furthermore, the shale may still be largely intact in the local area of the sample even after it has cracked overall, and frictional resistance still exists between the fragments. These reasons lead to a certain compressive strength even after the entire shale has ruptured.

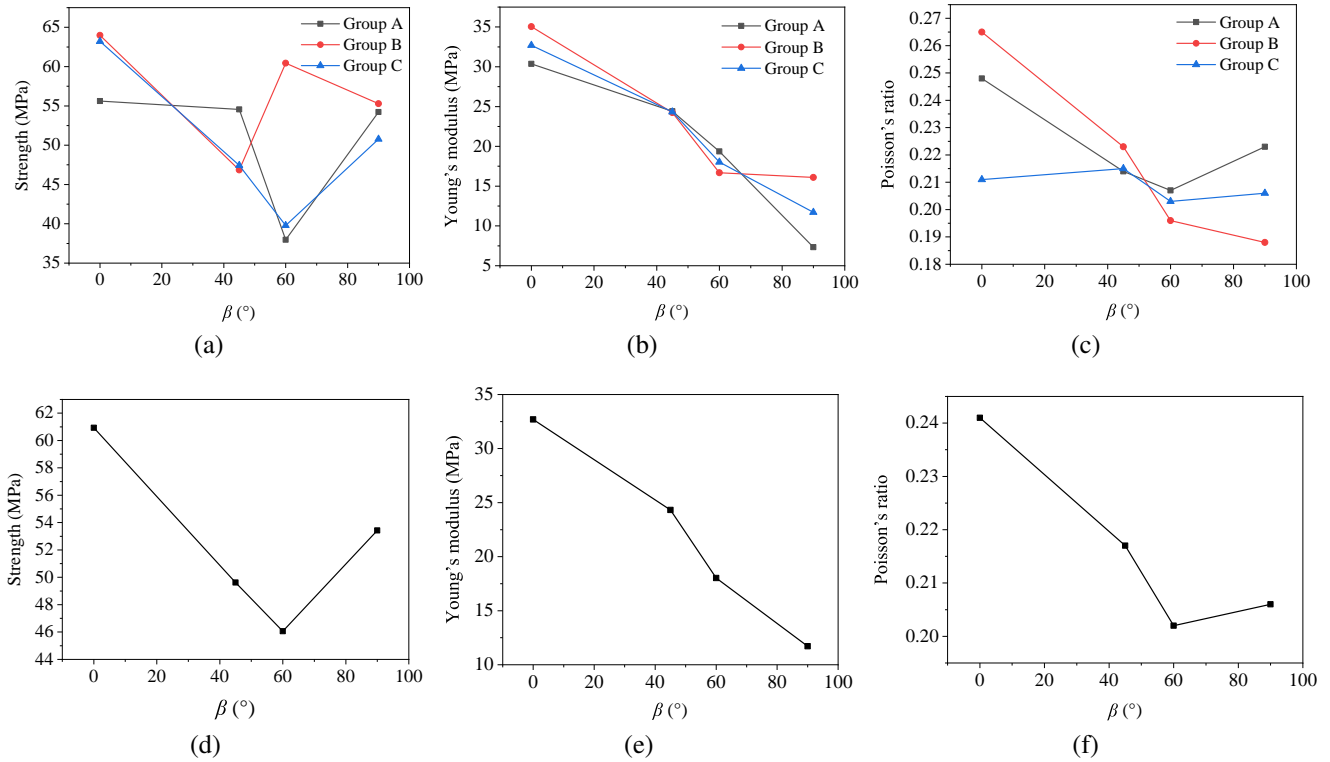


Fig. 5. The curves of each mechanical parameter versus β . (a) The curve between uniaxial compressive strength and β , (b) the curve of Young's modulus and β , (c) the curve of Poisson's ratio and β , (d) the curve of the average uniaxial compressive strength and β , (e) the curve of the average Young's modulus and β and (f) the curve of the average Poisson's ratio and β for the three groups of samples.

In addition, the test results illustrate that the compression strength of shale is at its highest when $\beta = 0^\circ$. Meanwhile, the sample has the lowest compressive strength at $\beta = 60^\circ$ (Fig. 4), because this is a significant angle formed between the lamination surface and the load. Shear damage will occur preferentially in the location due to the significantly lower cementation degree of the lamination surface than other shale portions, which goes hand in hand with the previously described damage mode (Gholami and Rasouli, 2014). The sample approaches radial tensile damage at $\beta = 0^\circ$, when the lamination surface is perpendicular to the load. Otherwise, the lamination surface has less of an impact.

3.3 Analysis of shale mechanical parameters

The uniaxial compressive strength of the three groups of samples shows a steady drop with increasing β after the experiment (Fig. 5). The uniaxial compressive strength achieves its minimal value at $\beta = 60^\circ$, which is an average of 46.063 MPa. Subsequently, it progressively rises as β increases, and the entire curve is low in the middle and high at both ends of the variation law. The test results show that the Young's modulus of the three sample groups falls as β increases, and the whole curve exhibits a positive linear decreasing law, with the pattern of change being the same as that indicated by other studies (Arora and Mishra, 2015; Niloufar and Fatemeh, 2023).

The Poisson's ratio increases as β rises and then progres-

sively falls, reaching a minimum of 0.207 at $\beta = 60^\circ$ in group A. Then, the Poisson's ratio gradually grows as β increases. The Poisson's ratio of group B has a decreasing tendency and is inversely proportional to β , and that of group C barely varies as β rises. However, average values of the three Poisson's ratios exhibit a declining tendency along the curve. This is almost in line with the findings of previous studies (Arora and Mishra, 2015; Marie et al., 2019; Niloufar and Fatemeh, 2023).

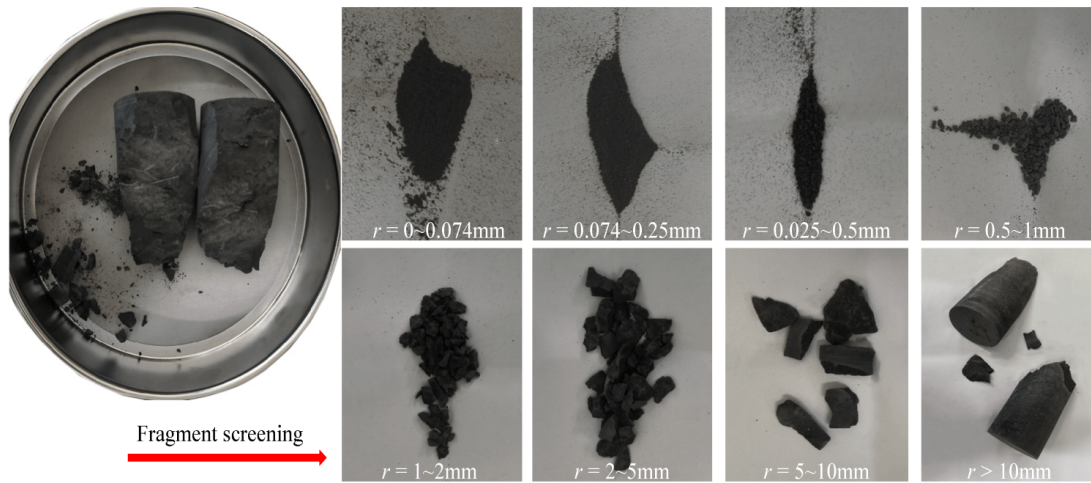
3.4 Calculation of block fractal dimension

The fragmentation characteristics of rock samples were determined by using the sieve method on the damaged shale fragments, which were sorted by serial number following the uniaxial compression tests. According to the fragment classification method of He et al. (2014), the fragments generated from each shale sample were sieved using experimental sieves with aperture sizes of 0.074, 0.25, 0.5, 1, 2, 5 and 10 mm. The masses of fragments produced by each sieve were measured separately, to obtain the values for different particle size groups of all shale samples, as shown in Fig. 6 and Table 2.

Taking the block size distribution model of rock fragmentation $N = cr^{-D}$ (Rickman et al., 2008; Sahimi, 2011) and the R-R (Rosin-Rammler) (Rickman et al., 2008; Li, 2014) distribution function, it is possible to obtain the formula for the fractal dimension calculation of the mass-characteristic size of the fragmented blocks:

Table 2. Mass distribution of shale sample fragments.

Samples	Total mass of debris (g)	Particle size (mm)							
		0-0.074	0.074-0.25	0.25-0.5	0.5-1	1-2	2-5	5-10	> 10
A1	507.898	0.132	0.230	0.146	0.185	0.665	1.843	3.097	501.600
A2	497.943	0.048	0.084	0.067	0.128	0.423	0.700	4.543	491.950
A3	510.029	0.156	0.673	0.749	1.880	3.857	8.702	24.044	469.968
A4	503.114	0.026	0.065	0.085	0.154	0.574	0.888	0.752	500.570
B1	502.011	0.083	0.163	0.155	0.247	0.658	0.712	3.720	496.273
B2	500.917	0.023	0.068	0.071	0.123	0.261	0.341	0.585	499.445
B3	505.013	0.031	0.085	0.106	0.150	0.399	1.286	3.283	499.673
B4	504.021	0.017	0.052	0.062	0.110	0.301	1.020	6.555	495.904
C1	502.392	0.009	0.023	0.024	0.045	0.134	0.283	0.256	501.618
C2	496.233	0.025	0.047	0.052	0.099	0.303	0.754	0.905	494.048
C3	507.147	0.049	0.113	0.157	0.268	0.821	1.945	8.926	494.868
C4	511.392	0.079	0.134	0.138	0.230	0.578	1.702	6.850	501.681

**Fig. 6.** Sample A2 with different particle sizes.

$$D_1 = 3 - k \quad (1)$$

$$k = \frac{\lg \frac{M(r)}{M}}{\lg r} \quad (2)$$

where k represents the slope of the straight line of the function in double log $\lg(M(r)/M)$ coordinates (Sui et al., 2016); $M(r)$ represents the cumulative mass of fragments with characteristic dimensions less than r ; M represents the total mass of the shale samples. From the above Eqs. (1) and (2), the block fractal dimension D_1 of each group of rocks can be calculated.

The R^2 values of the fitting line are higher than 0.98, indicating that there is a significant degree of self-similarity and fractal characteristics among the fragments (Fig. 7).

The above results clearly illustrate how the lamination

angle affects the fractal dimension, displaying a progressive diminishing trend as β increases from 0° to 45° exhibiting strong regularity (Figs. 8(a)-8(b)). It is evident that a stronger trend of decreasing fractal dimension is required when increasing β from 45° to 60° compared to 0° to 45° . However, the fractal dimension increases in the opposite direction when β increases from 60° to 90° .

Mechanical compression studies have revealed a strong linear relationship between the fractal size of rock pieces and the mechanical characteristics of rock (Bagde et al., 2002; Xu et al., 2023). The correlation coefficients achieved in this paper are 0.6214, 0.7115 and 0.7569 (the red data points in Figs. 8(d)-8(f) are points with strong discreteness, and the correlation changes between 0.1-0.2 after removal), whereas the correlation coefficients acquired by previous studies are all above 0.8 (Bagde et al., 2002; Xu et al., 2023). The rationale

behind this discrepancy is that earlier researchers employed mudstone and sandstone samples with better homogeneity, obtaining more ideal results. However, it is clear that the fractal dimension of shale strongly correlates with its mechanical properties.

In order to more intuitively analyze the effect of lamination angle β on the degree of shale damage, the block size distribution coefficient α (Li, 2014) was defined to characterize the degree of sample fragmentation, and it is calculated as follows:

$$\alpha = \sum_{i=1}^8 W_i \bar{r}_i \quad (3)$$

where W_i represents the percentage of fragment size to the overall mass under each particle size, \bar{r}_i indicates the average particle size of the i group size range, which is the average of the maximum particle size and the minimum particle size within the size range (the ≤ 5 mm group is taken as the average value of the aperture of the sieve mesh, such as 0-0.074 mm is taken as 0.037 mm). According to the definition, α represents the average particle size of the fragments after the rock sample is damaged. The smaller the value of α , the higher the degree of damage.

Furthermore, the calculation results indicate that the value of α is relatively large for $\beta = 45^\circ$ and 60° (Fig. 8(c)), which is consistent with the mode of damage. According to previous research, the block fractal dimension can visualize the damage degree of rock (Li, 2014). From an energy perspective, the lamination surface forms a significant angle with the loading direction when $\beta = 45^\circ$ and 60° . It takes less energy to cause the lamination surface to shear slide preferentially because the degree of cementation here is significantly lower than that in other sample components. Therefore, samples produce few but massive fragments. In contrast, for $\beta = 0^\circ$ and 90° , more energy is required to make the extended cracks sprout inside the sample. The result is further damage and intricate cracks, producing plenty of small fragments.

3.5 Calculation of crack fractal dimension

The crack fractal dimension following the damage of shale samples with different lamination angles was determined using the box dimension approach, which was based on the calculation of block fractal dimension. The following formula was used to determine the crack fractal dimension (Boris et al., 2021; Wang et al., 2023):

$$D_2 = \lim_{i \rightarrow \infty} \frac{\ln N_{r_i}(F)}{-\ln r_i} \quad (4)$$

where D_2 represents the number of box dimensions; r_i represents the side length of the square box, mm; N_{r_i} represents the number of boxes required to cover the entire region in the photo, where cracks are present with a square box with side length r_i .

3.5.1 Calculation of crack fractal dimension from post-experimental photographs

The cracks of the experimental shale ruptures were photographed and saved to facilitate calculating the fractal dimensions for relevant cracks later on. We employed Image J and

CorelDRAW image processing software to binarize and cover the principal cracks associated with each shale sample. The side lengths of the square boxes in the order were 5, 10, 15 and 20 mm (Fig. 9).

The fitting results show that the correlation of $\ln N_r - \ln r$ curve is excellent. The mean value is greater than 0.95, thereby the main cracks of the sample have a high degree of self-similarity (Fig. 10). The calculations for D_2 display how the fractal dimension of the sample crack decreases by 0.066 when β increases from 0° to 60° . The crack fractal dimensions under the uniaxial compression of shale indicate a change with increasing lamination angle, becoming low in the middle and high at both ends. The results presented in this paper are consistent with earlier research on the fractal properties of surface cracks in rock samples (Wang et al., 2023). The crack fractal dimensions have a certain discreteness because of the significant heterogeneity of shale. However, a positive correlation can also be observed between the fractal dimension and compression strength of shale. The sample with $\beta = 0^\circ$ has a lamination surface that is perpendicular to the direction of loading, which shows mainly radial tensile deformation; therefore, it is mainly subjected to tensile tension and has the greatest compressive strength. As a result, the resulting cracks are complex and this sample is most severely damaged. However, samples with $\beta = 60^\circ$ exhibit a large angle between the lamination surface and the loading direction. The lamination surface will preferentially undergo slip shear damage relative to other regions of the sample. The whole sample is almost damaged into two major parts of diagonal cut type. The resulting crack is fairly large and runs through the sample; therefore, this sample has the lowest degree of damage as well as the lowest compressive strength and crack fractal dimension.

3.5.2 Calculation of crack fractal dimension by CT scanning

In order to quantitatively characterize the cracks in the samples more comprehensively, typical samples with more complete preservation after the uniaxial compression experiments were selected for the CT scanning experiments. Based on the coordinate axes of the CT scanning, the upper end face, the middle section, the lower end face, the face with varying angles (0° , 45° and 90°) between the sections, and their x -axes were chosen to statistically calculate the crack fractal dimensions. Then, the cracks were identified and segmented by Convex Hull of Image J and the box dimensions were counted by CorelDRAW image processing software (Fig. 11) (González-Tello et al., 2008; Peng et al., 2011).

The results indicate that the cracks of each section have excellent self-similarity ($R^2 > 0.95$) (Fig. 12). Moreover, the fractal dimension D_2 with β for the principal cracks in the central section and the sections with 0° , 45° and 90° angles to the x -axis present a very similar trend (Fig. 13). The fractal dimension D_2 also reaches its lowest value at $\beta = 60^\circ$, which is 0.931, 0.869, 1.09, 1.082, respectively, while it reaches the maximum value of 1.306, 1.373, 1.242, 1.213, respectively, at $\beta = 0^\circ$. The curves exhibit non-linearity, with low in the middle and high at both ends of the variation law, nearly

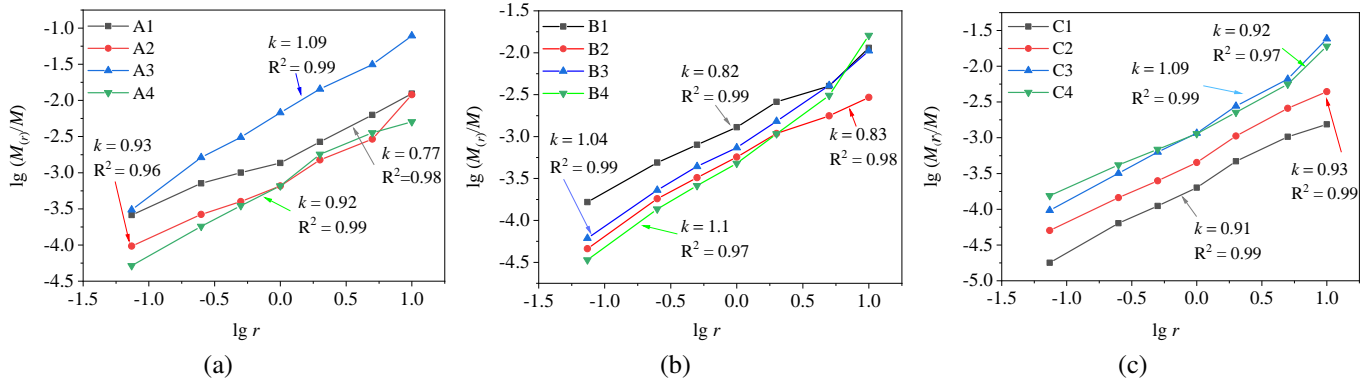


Fig. 7. The $\lg r - \lg(M(r)/M)$ fitting curve of (a) all samples in group A, (b) all samples in group B and (c) all samples in group C.

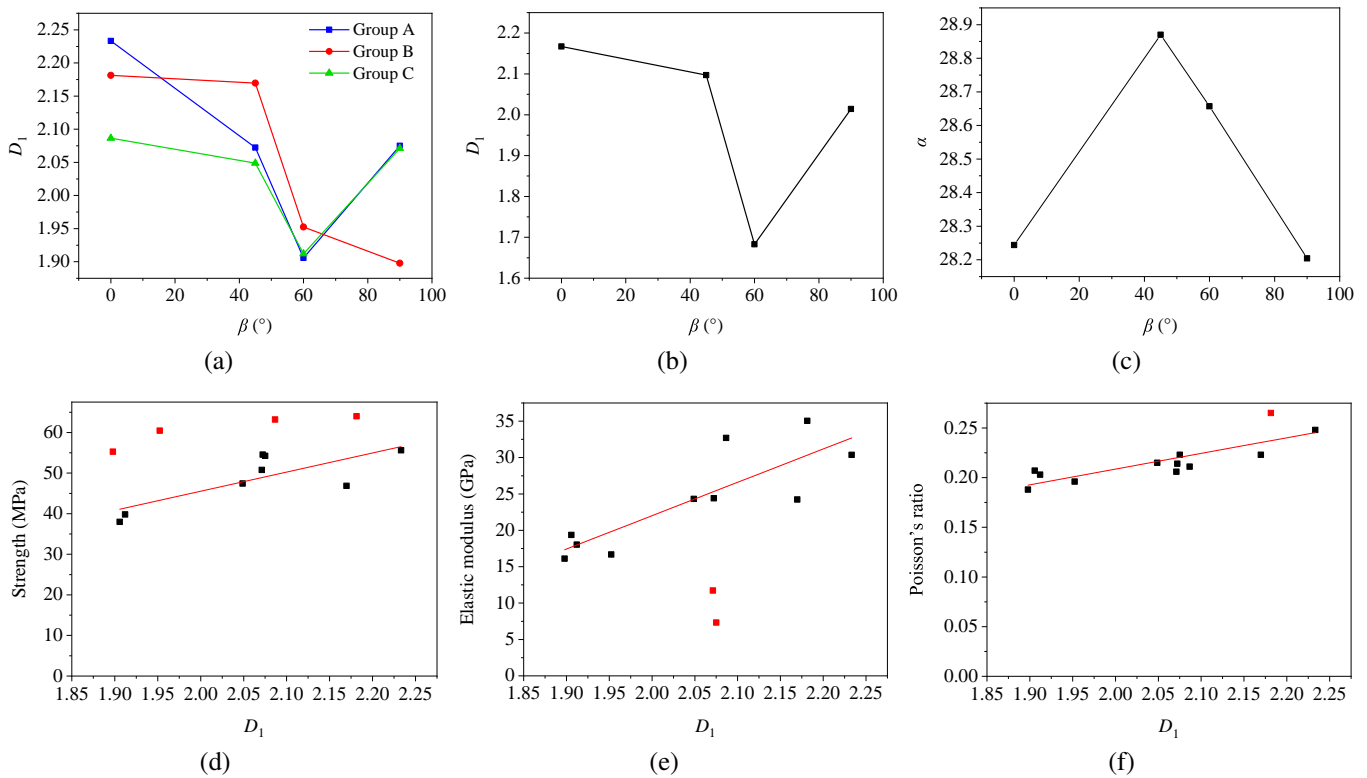


Fig. 8. Relationships between parameters. (a) The relationship curve between fractal dimension and β for three groups of samples, (b) the relationship curve between the average fractal dimension of the three groups of samples and β , (c) plot of α versus β , (d) fitting curve of D_1 and uniaxial compressive strength, (e) fitting curve of D_1 and Young's modulus and (f) fitting curve of D_1 and Poisson's ratio.

perfectly matching the preceding chapter and corresponding to the pattern of the cracks appearing at $\beta = 60^\circ$ in earlier chapters. The fractal dimension D_2 of the main crack at the upper end face exhibits an overall decreasing trend with increasing β . However, the fractal dimension D_2 reaches its maximum value of 1.122 at $\beta = 45^\circ$. The computation of the crack fractal dimension is hampered by the upper end of the low-resolution CT scan. The overall curve trend is nearly identical to that of others.

In contrast to the other end faces, the fractal dimension D_2

of the main crack at the lower end face reaches its maximum value of 1.172 at $\beta = 90^\circ$. The crack fractal dimension has a nonlinear relationship with β . The highest and lowest values of β differ significantly from those of the other end faces. This is probable because during the uniaxial compression test, the load is applied from the axial base upward. Therefore, the bottom of the shale sample is more severely damaged. Furthermore, the lower end surface has the greatest number of lamination surfaces when $\beta = 90^\circ$. The cracks that expand along the lamination surface are more developed, resulting in

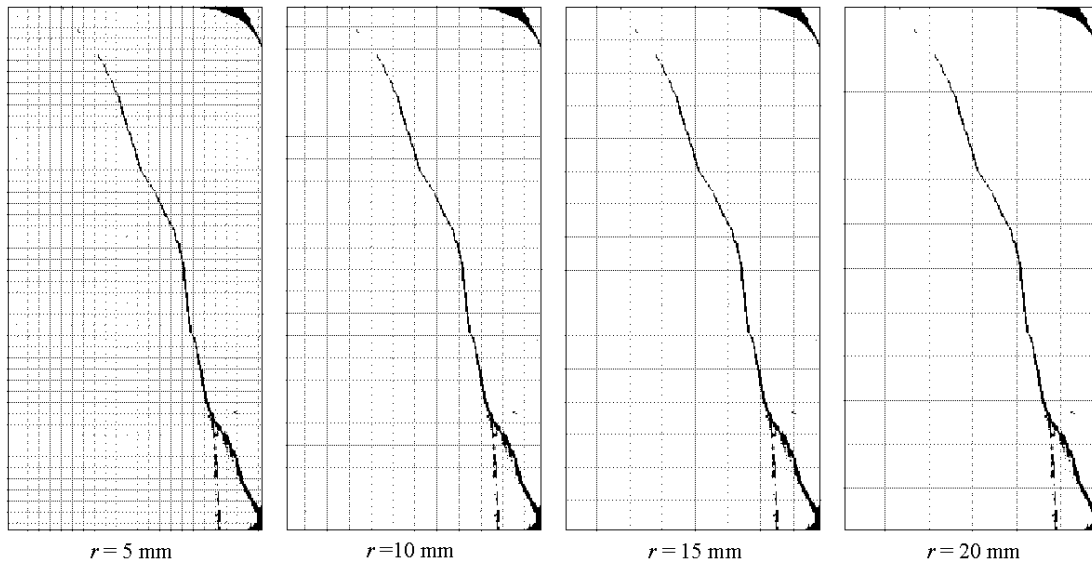


Fig. 9. The process of A3 cracks being covered by boxes of different side lengths.

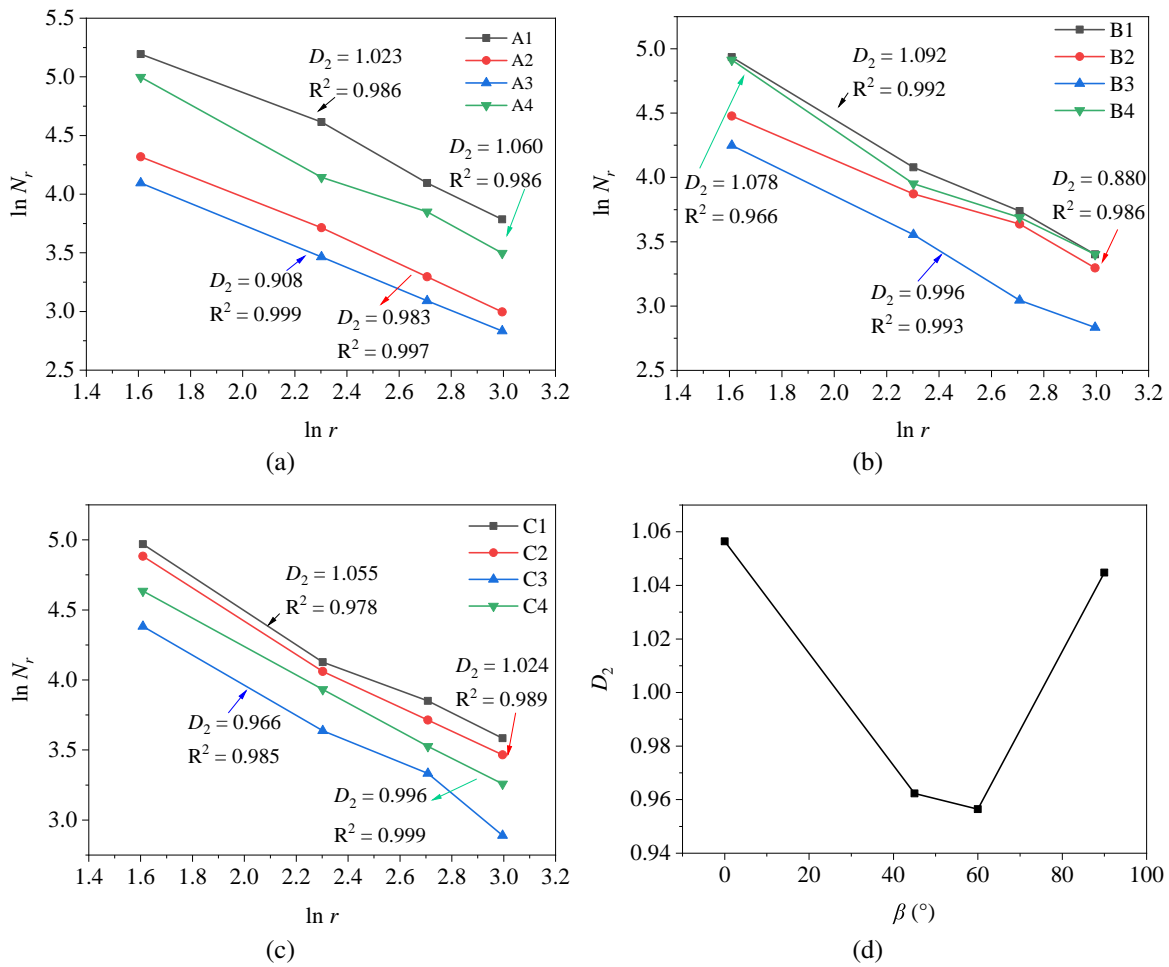


Fig. 10. Plot of $\ln N_r$ - $\ln r$ curve fit for all samples. (a) The $\ln N_r - \ln r$ fitting curve of group A samples, (b) group B samples, and (c) group C samples and (d) the average of crack fractal dimensions in the three groups of samples at different lamination angles.

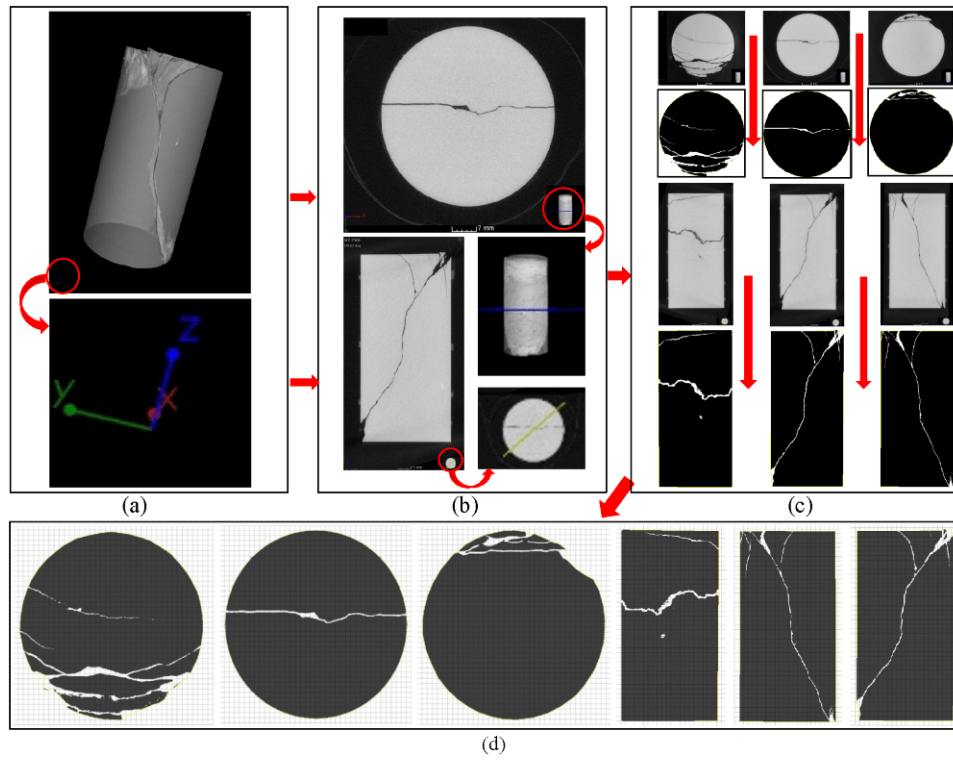


Fig. 11. CT three-dimensional reconstruction of section capture process. (a) The sample CT three-dimensional reconstruction model and its own coordinate axis, (b) the section of the sample derived from the three-dimensional model, (c) crack identification on CT scan photographs of selected samples and (d) the counting process of box dimension when $r = 5$ mm.

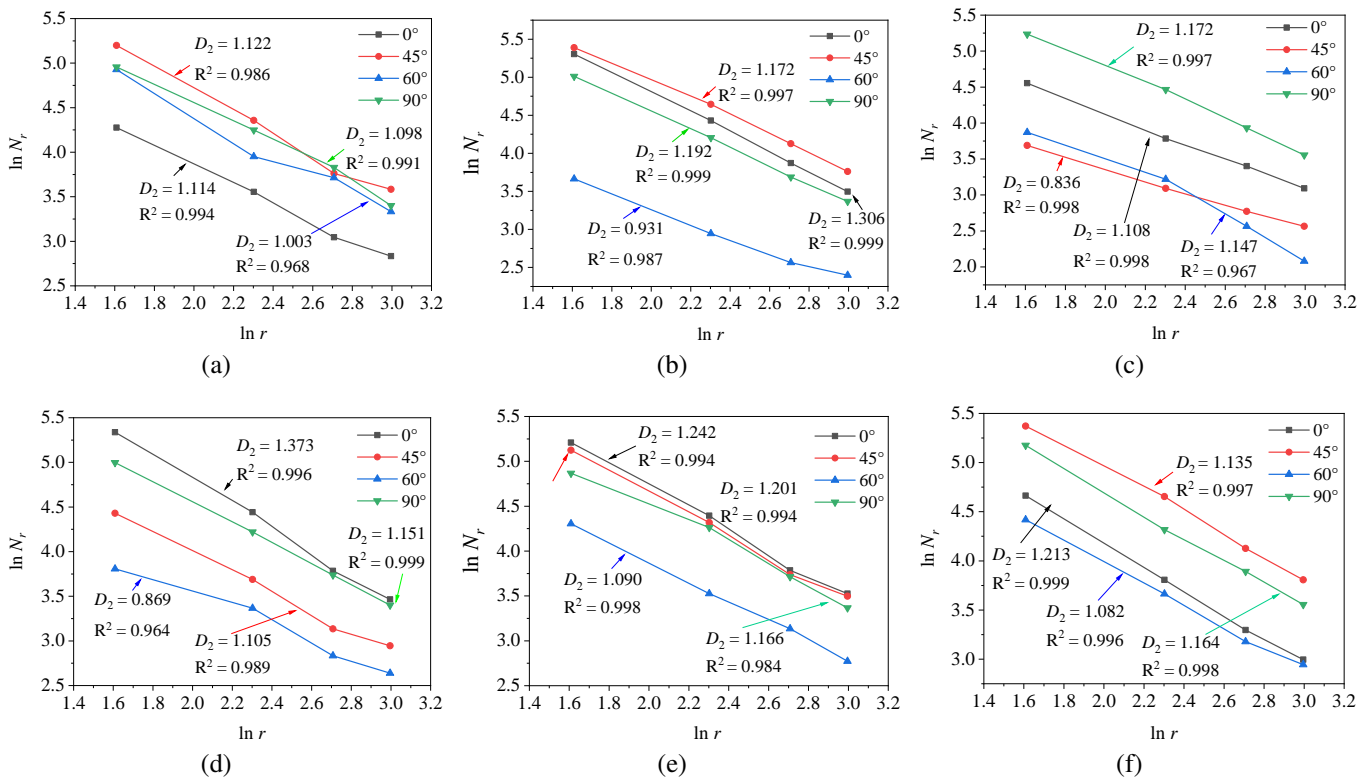


Fig. 12. Plot of $\ln N_r - \ln r$ curve fit for each cross section for all samples. (a) Upper surface, (b) central section, (c) lower face, (d) cross-section angle 0° to x -axis, (e) cross-section angle 45° to x -axis and (f) cross-section angle 90° to x -axis.

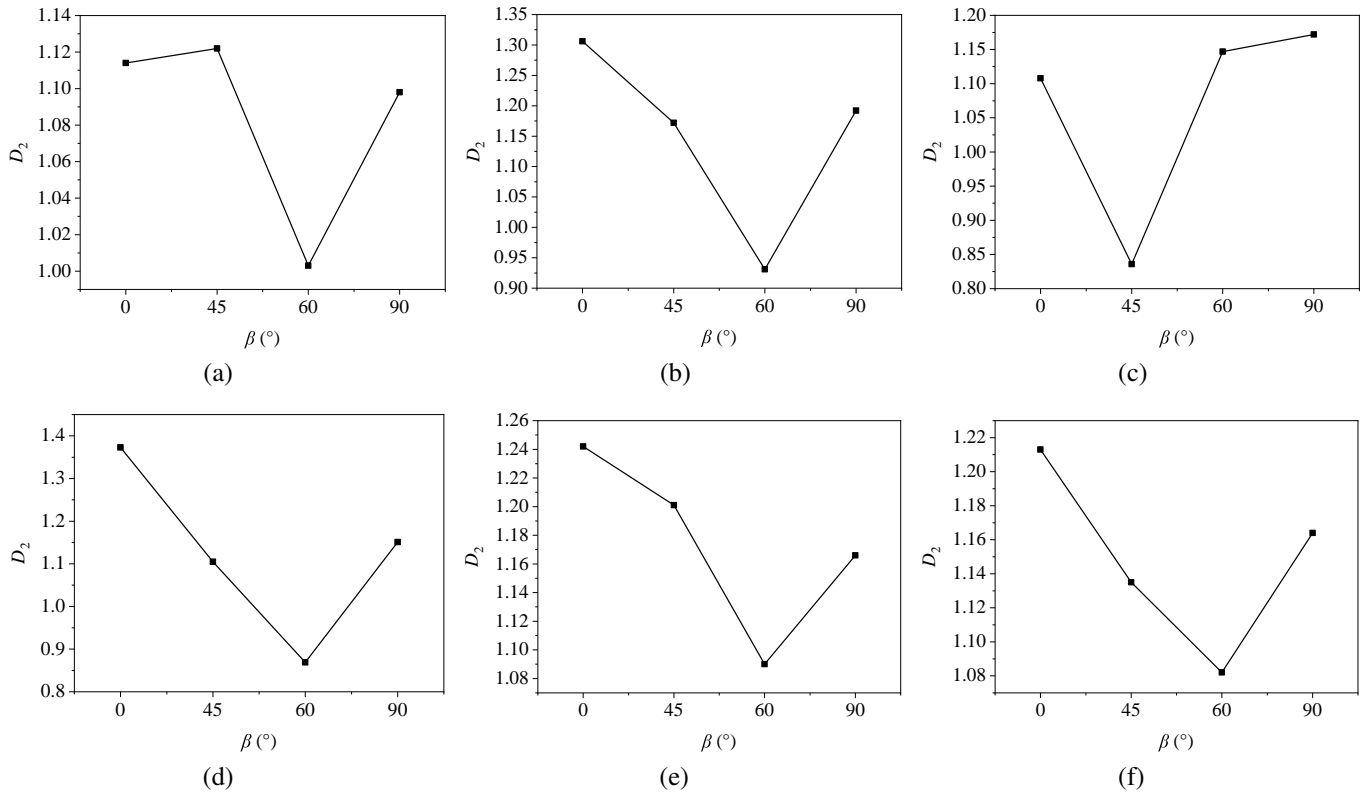


Fig. 13. Fractal dimension-lamination angle β relationship for each cross section for all samples. (a) Upper surface, (b) central section, (c) lower face, (d) cross-section angle 0° to x -axis, (e) cross-section angle 45° to x -axis and (f) cross-section angle 90° to x -axis.

more damage than at other β values.

Both fractal dimensions of the cracks produced in this paper present almost the same pattern of variation with β , which have a certain fitting relationship with their mechanical parameters. Shale damage causes more cracks at $\beta = 0^\circ$ and 90° , which in turn causes the cracks to become more complicated and the peeling off of more fragments from the crack network. Alternatively, the shale-produced cracks are close to shear cracks through at $\beta = 45^\circ$ and 60° , meaning that fewer fragments peel off along the cracks. Both of these are favorably linked with one another.

The above results further indicate that even if the shale has strong heterogeneity, the cracks inside and outside it has high self-similarity, so the fractal dimension can accurately quantify them. This is consistent with the physical meaning of fractal dimension (Li, 2014): A larger fractal dimension represents a higher degree of self-similarity of the crack, a more complex crack morphology and more energy required for crack sprouting and expansion. Overall, the crack fractal dimension can describe the shale damage morphology and its correlation with the mechanical parameters both quantitatively and energetically, explaining the damage process.

4. Conclusions

Based on the results of uniaxial compression experiments performed on shale samples from the Silurian Longmaxi Formation, Sichuan Basin, and the structural observations of

deformed samples, the following conclusions may be drawn:

- 1) Three damage modes are identified in the shale by mechanical tests: Shear, tension-shear, and tension. The direction of loading and lamination causes regular changes in the mechanical characteristics of samples. The compressive strength diminishes nonlinearly as the lamination angle increases, whereas Young's modulus and Poisson's ratio are almost inversely proportional to the lamination angle.
- 2) The block fractal dimension and crack fractal dimension are calculated by using post-experimental photographs and CT images, realizing the quantitative evaluation of rock damage and the investigation of shale mechanical properties.
- 3) The fractal dimensions are useful to accurately describe damage patterns and relate them to mechanical properties, which contributes to the understanding of shale damage evolution.

Acknowledgements

This research was financially supported by the National Natural Science Foundation of China (No. 42102186), the Hebei Natural Science Foundation (No. D2023203008) and the Science Research Project of Hebei Education Department (No. BJK2022018). All the editors' and anonymous reviewers' contributions are gratefully acknowledged.

Conflict of interest

The authors declare no competing interest.

Open Access This article is distributed under the terms and conditions of the Creative Commons Attribution (CC BY-NC-ND) license, which permits unrestricted use, distribution, and reproduction in any medium, provided the original work is properly cited.

References

- Alex, V., Ahmad, G. Damage characteristics of three shales under true-triaxial compression. *International Journal of Rock Mechanics and Mining Sciences*, 2017, 100: 151-159.
- Amir, B. Y., Andy, W., Patrick, F. Application of a density-volume fractal model for rock characterisation of the Kahang porphyry deposit. *International Journal of Rock Mechanics and Mining Sciences*, 2014, 66: 188-193.
- Arora, S., Mishra, B. Investigation of the failure mode of shale rocks in biaxial and triaxial compression tests. *International Journal of Rock Mechanics and Mining Sciences*, 2015, 79: 109-123.
- Bagde, M. N., Raina, A. K., Chakraborty, A. K., et al. Rock mass characterization by fractal dimension. *Engineering Geology*, 2002, 63(1-2): 141-155.
- Boris, G., Anna, G., Evgenij, K., et al. Strength equation of composite materials and fractal dimension of cracks. *Energy Reports*, 2021, 7(5): 569-578.
- Gao, J., Li, X., Cheng, G., et al. Structural evolution and characterization of organic-rich shale from macroscopic to microscopic resolution: The significance of tectonic activity. *Advances in Geo-Energy Research*, 2023, 10(2): 84-90.
- Gholami, R., Rasouli, V. Mechanical and elastic properties of transversely isotropic shale. *Rock Mechanics and Rock Engineering*, 2014, 47(5): 1763-1773.
- González-Tello, P., Camacho, F., Vicaria, J. M., et al. A modified Nukiyama-Tanasawa distribution function and a Rosin-Rammler model for the particle-size-distribution analysis. *Powder Technology*, 2008, 186(3): 278-281.
- He, M., Zhao F., Du S., et al. Experimental analysis of rock burst damage characteristics under different unloading rates. *Rock and Soil Mechanics*, 2014, 35(10): 2737-2747 + 2793. (in Chinese)
- Li, G., Jin, Z., Li, X., et al. Experimental study on mechanical properties and fracture characteristics of shale layered samples with different mineral components under cyclic loading. *Marine and Petroleum Geology*, 2023, 150: 106114.
- Li, M. Research on damage and crack mechanism of coal measure sandstone under high temperature and impact load. Xuzhou, China University of Mining and Technology, 2014. (in Chinese)
- Li, Y., Song, L., Tang, Y., et al. Evaluating the mechanical properties of anisotropic shale containing bedding and natural fractures with discrete element modeling. *International Journal of Coal Science & Technology*, 2022, 9(2): 16.
- Liu, B., Wang, S., Ke, X. Mechanical characteristics and factors controlling brittleness of organic-rich continental shales. *Journal of Petroleum Science and Engineering*, 2020, 194: 107464.
- Mandelbrot, B. B. The fractal geometry of nature. *American Journal of Physics*, 1983, 51(3): 286-286.
- Marie, L. T. D., Morteza, N., Daniel, V. On the direct measurement of shear moduli in transversely isotropic rocks using the uniaxial compression test. *International Journal of Rock Mechanics and Mining Sciences*, 2019, 113: 220-240.
- Niloufar, M., Fatemeh, M. Theoretical and experimental investigation of a shear failure model for anisotropic rocks using direct shear test. *International Journal of Rock Mechanics and Mining Sciences*, 2023, 170: 105561.
- Peng, R., Yang Y., Ju, Y., et al. Calculation of fractal dimension of rock pores based on gray-scale CT images. *Chinese Science Bulletin*, 2011, 56(26): 2256-2266. (in Chinese)
- Rickman, R., Mullen, M., Petre, E., et al. A practical use of shale petrophysics for stimulation design optimization: All shale plays are not clones of the Barnett Shale. Paper SPE 115258 Presented at the SPE Annual Technical Conference and Exhibition, Denver, Colorado, USA, 21-24 September, 2008.
- Rybacki, E., Reinicke, A., Meier T., et al. What controls the mechanical properties of shale rocks?-Part I: Strength and Young's modulus. *Journal of Petroleum Science and Engineering*, 2015, 135: 702-722.
- Sahimi, M. *Flow and Transport in Porous Media and Fractured Rock: From Classical Methods to Modern Approaches*. Weinheim, Germany, John Wiley & Sons, 2011.
- Sarout, J., Molez, L., Guéguen, Y., et al. Shale dynamic properties and anisotropy under triaxial loading: Experimental and theoretical investigations. *Physics and Chemistry of the Earth*, 2007, 32(8-14): 896-906.
- Sethi, C., Hazra, B., Ostadhassan, M., et al. Depositional environmental controls on mechanical stratigraphy of Barakar Shales in Rajmahal Basin, India. *International Journal of Coal Geology*, 2024, 285: 104477.
- Sui, L., Ju, Y., Yang, Y., et al. A quantification method for shale fracability based on analytic hierarchy process. *Energy*, 2016, 115: 637-645.
- Su, Y., Sun, Q., Wang, W., et al. Spontaneous imbibition characteristics of shale oil reservoir under the influence of osmosis. *International Journal of Coal Science & Technology*, 2022, 9(5): 48-58.
- Velde, B., Dubois, J., Moore, D., et al. Fractal patterns of fractures in granites. *Earth and Planetary Science Letters*, 1991, 104(1): 25-35.
- Wang, H., Cui, Y., Yuan, G., et al. Fractal characteristics of granite with different weathering degrees based on uniaxial compression test. *Rock and Soil Mechanics*, 2023, 44(8): 2249-2265. (in Chinese)
- Xiao, C., Yang, R., Ma, X. Damage evaluation of rock blasting based on multi-fractal study. *International Journal of Impact Engineering*, 2024, 188: 104953.
- Xu, S., Yang, H., Li, L., et al. Real-time evaluation method of rock mechanical parameters based on rock chip frac-

- tal theory. *Science Technology and Engineering*, 2023, 23(32): 13803-13810. (in Chinese)
- Zhao, L., Mao, W., Liu, Z., et al. Research on the differential tectonic-thermal evolution of Longmaxi shale in the southern Sichuan Basin. *Advances in Geo-Energy Research*, 2023, 7(3): 152-163.
- Zhao, Q., Yang, S., Wang, H., et al. China's shale gas development and its prospects. *Environmental Impact Assessment*, 2019, 41(1): 6-10. (in Chinese)
- Zhu, H., Huang, C., Ju, Y., et al. Multi-scale multi-dimensional characterization of clay-hosted pore networks of shale using FIBSEM, TEM, and X-ray micro-tomography: Implications for methane storage and migration. *Applied Clay Science*, 2021, 213: 106239.